This article has been accepted for publication in IEEE Transactions on Mobile Computing. This is the author's version which has not been fully edited and content may change prior to final publication. Citation information: DOI 10.1109/TMC.2024.3442439

Ubiquitous Indoor Mapping using Mobile Radio Tomography

Amartya Basu, Ayon Chakraborty, Kush Jajal

Abstract—The demand for real-time and accurate mapping is ubiquitous, particularly in complex indoor settings. While SLAM-based methods are popular, Radio Tomographic Imaging (RTI) offers an essential set of advantages, including mapping inaccessible or enclosed spaces, shorter scanning trajectories, or even identifying material properties of structures on the map. However, existing RTI systems typically depend on pre-deployed, precisely calibrated infrastructure with ample computing power, making it challenging to deploy in a ubiquitous setting. We design UBIQMAP, a lightweight RTI-based end-to-end system capable of mapping indoor spaces in real-time, with minimal to zero reliance over pre-deployed infrastructure. We evaluate the performance of UBIQMAP in various scenarios, including two real deployments - a moderately complex residential apartment (800 sq. ft) and a large building foyer area (3000 sq. ft) and a few simulated scenarios. We demonstrate how UBIQMAP can benefit over traditional SLAM-based techniques in specific contexts and advocate the fusion of RTI methods with SLAM to improve future mapping technologies. Overall, UBIQMAP improves the quality of the estimated map by 30%–40% over the state-of-the-art with equivalent resource availability.

Index Terms—Indoor mapping, wireless imaging, tomography

1 INTRODUCTION

Mapping indoor spaces in real-time is still considered a challenging task [1], [2], and more so without access to pre-deployed infrastructure. Such challenges amplify in public safety scenarios [3] where not only infrastructure is unreliable or infeasible to deploy, but also the environment is dynamic – varying ambient conditions, uncontrolled or fast movements and so on [4], [5]. To bolster the criticality of the challenge, we analyze quotes from over 20K first responders capturing their field experiences (NIST dataset [6]). About 43% of the quotes refer to the unavailability of maps, unknown building layouts, navigation issues and related mapping challenges.

In this paper, we design, deploy and evaluate UBIQMAP, an end-to-end system capable of mapping indoor spaces in real-time, with minimal or zero reliance over pre-deployed infrastructure, predominantly targeting time-critical, resource-constrained environments like first responder scenarios. Essentially, such a mapping process has two critical requirements: (i) *sensing building structures* (e.g., obstacles, walls) along with estimating their relative positions from the sensor's location, and (ii) *tracking location coordinates* of the sensing system to bind the sensed structures to physical space. UBIQMAP employs Radio Tomographic Imaging (RTI), a wireless sensing technique that estimates RF attenuation over an area of interest. In the following, we motivate RTI as a candidate indoor mapping approach, particularly in non-line-of-sight (NLOS) scenarios.

Limitations of SLAM. Simultaneous Localization and Mapping or SLAM-based algorithms have been widely adopted for various mapping tasks. However, they have their limitations [5]. First, the sensing modalities typical of SLAM (lidar, acoustic, mm-wave, visual/camera-based), although precise, are only suitable to sense structures in direct Line-of-Sight (LOS) that enforce longer scanning trajectories and hence longer duration for the mapping process. Second, SLAM-based maps are solely restricted to spatial regions explored by the sensory agent. Areas that are not physically accessible are excluded from the map. Third, SLAM algorithms require orchestrated and accurate (robot-like) movement by the sensory agent. Such precise orchestration and control is infeasible, especially when we leverage natural human movements to achieve sensor mobility – for instance, body-worn sensors by first responders [7], [8]. Some recent bodies of work, for example, Topology SLAM or their neural counterparts [9], [10], [11] do away with such restrictions. However, they introduce compute heavy tasks that are infeasible to realize on portable devices. Fourth, it is rather impossible to infer the material properties of obstacles, for instance, telling apart a concrete wall from a drywall. Such information, if available, can be of premium for many applications, e.g., search and rescue. Fig. 1 captures the crucial benefits of RTI over traditional SLAM. Not only that the enclosed spaces are mapped, but also the RTI based map

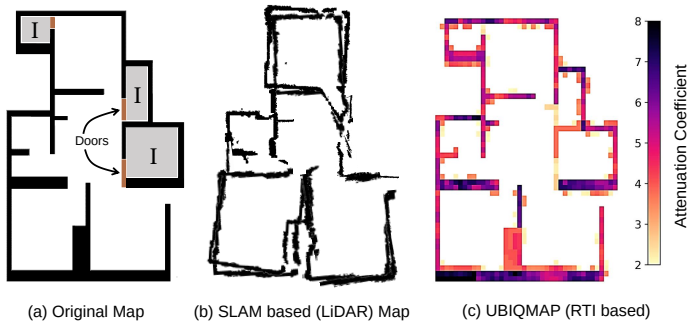

(a) Original Map (b) SLAM based (LiDAR) Map (c) UBIQMAP (RTI based)

Fig. 1: (*a*) Layout of an indoor space with inaccessible areas shaded, marked '`I`' (*b*) SLAM based reconstruction of the area using a mobile robot (*c*) UBIQMAP's RTI based estimation of the layout structure. The attenuation coefficient roughly depicts the material properties of the structure - e.g., brick wall, wood etc.

provides additional details, including the thickness of the structures or their material properties (more on this later)

Mapping Beyond Line-of-Sight (LoS). Methods in Radio Tomographic Imaging (RTI) [12], [13], [14], [15] benefit by the use of radio frequencies (RF), typically in the sub-6 GHz spectrum, that can potentially penetrate through building structures and 'see' beyond LoS. RTI algorithms essentially estimate the wireless attenuation coefficient map (*aka*, attenuation image), i.e., the extent by which the RF signal power degrades at every point within the region of interest. It is evident that such an attenuation map strongly correlates to the region's occupancy map or structural layout. For instance, concrete walls or other building structures have appreciably higher attenuation coefficients as compared to free space. RTI algorithms use a set of spatially distributed transmitter-receiver pairs at known locations, where each pair records the total wireless attenuation or propagation loss from the transmitter to the receiver.

Given the attenuation image, using standard wireless fading models [16], [17] it is relatively straightforward to estimate the total propagation loss between any two points on the map (aka, *forward problem*), albeit approximately. However, RTI attempts to solve the *inverse problem*. Propagation loss measurements from localized transceivers are used to estimate the attenuation image and hence, the structural layout. Note that such inverse problems are ill-posed in nature (see [18], [19], more on this later). Their solutions, i.e., the attenuation images vary drastically with slight variations in the input parameters, i.e., transceiver locations and channel estimates. This follows that the accuracy of the transceiver location and the wireless channel estimates critically determine the performance of a RTI system [20], a significant challenge in dynamic indoor environments.

We propose UbiqMap, a portable wireless system that demonstrates the feasibility of RTI for mapping indoor structures in the wild. UbiqMap embraces the versatility of RF-based sensing to address the mapping problem in its entirety. Since deploying static transceivers or calibrating their precise locations is infeasible in our context, UbiqMap follows an infrastructure-free approach. In a nutshell, the system works as follows. We consider a set of mobile Wi-Fi transceivers (e.g., bodyworn radios) to perform distributed sensing. As the nodes traverse, the Wi-Fi transceivers continuously estimate and record their inter-nodal distances using the 802.11mc *Fine Time Measurement* [21] or *FTM* protocol, along with the Received Signal Strengths (RSS). The pair-wise range information is used to compute the relative topology of the nodes [22], which in turn assists in localizing the RSS measurements. Using such localized RSS measurements, the UbiqMap system reconstructs the obstacle map. In the following, we outline some key pain points that make it hard for such systems to be practically deployable.

Deployment Challenges. Although there has been a lot of analytical work [23], [15] and simulation studies [24] on RTI systems, end-to-end system demonstrations or empirical studies are limited. Among the ones that exist, either use a static set of transceivers at fixed, precisely known locations [12], [25], [26] or achieve transceiver mobility using highly sophisticated robotic maneuvering [27]. Towards our design for UbiqMap, we identify the following challenges that prohibit real world deployment of RTI solutions in time-critical and resource-constrained scenarios.

Computational challenges: RTI algorithms attempt to solve complex optimization problems where the computational resources or the latency required can be prohibitively high. For instance, the size of the optimization problem depends on the size of the measurement set as well as the resolution at which the map is reconstructed. Given that UbiqMap continually attempts to estimate and update the map in real-time, an important challenge is to understand the optimal resolution and how it trades off with the achieved accuracy and computation in the face of measurement noise.

Location uncertainty of transceivers: Although the mobile transceivers are continuously localized, it is well-known that the location estimates tend to be error prone. Unlike RSS noise, which is *additive*, such location error has a *multiplicative* effect, impacting the reconstruction accuracy drastically (more in Sec 3.1 and 4.3). Given the ill-posed nature of the RTI problem, a significant challenge is to embrace such location uncertainty into our algorithm without causing the mapping process to fail drastically. We make the following key contributions in this paper.

- UbiqMap estimates an optimal resolution for the attenuation image by trading off reconstruction quality versus compute load, while avoiding diminishing returns. This makes our system lightweight.
- We improve upon the robustness of the exiting RTI systems by embracing the *location uncertainty* of the RSS measurements and incorporating it directly into the RTI solution. UbiqMap can achieve nearly similar reconstruction quality using noisy Wi-Fi based location estimates as compared to its highly precise counterpart - a Ultra Wideband (UWB) based system.
- UbiqMap has been deployed and extensively tested in real-world complex environments, including an 800 sq. ft residential apartment and a 3000 sq. ft building foyer area. Our system not only improved upon the state-of-the-art baselines by 30–40% but was highly instrumental in mapping environments with *zero* indoor access or even highlighting material properties of the structures.

2 Related Work

Indoor mapping is a long standing problem and has been addressed in various degrees with a host of sensing modalities under multiple constraints (e.g., real-time, uncontrolled mobility, computation costs etc).

Visual, Acoustic or Inertial Sensing Based. Techniques utilizing visual sensing such as [28], [29], [30] works only within LoS ranges and depends heavily upon ambient lighting conditions. Acoustic techniques [31], [32] localize obstacles by using reflected sound waves, but are often erroneous when the sound source is relatively far from the target reflector and the area has a high degree of clutter. For instance, [32] utilizes sophisticated deep learning techniques requiring extensive training and numerous trials to estimate a reasonable map. In a very recent work [33], Conditional GAN (cGAN) is leveraged in to reconstruct

indoor maps using audio signals. The work requires extensive training as well as precise prior knowledge of the audio sensor's location, which limits its practicality. Mapping using crowdsourced inertial sensors (IMU) has been well explored [34], [35], however the limitations lie in the inherent noise introduced by the sensors themselves along with longer exploration/crowdsourcing time. In essence, in such cases, mapping becomes a biproduct of the localization process. State-of-the-art SLAM based techniques use one or more of the above modalities but require highly orchestrated and controlled movements, for instance using a robot [5], [27], [36], often infeasible in dynamic environments.

Wireless Solutions. A hold of RF-based (primarily, WiFi and other sub-6GHZ bands) systems [13], [37], [5], [38], [39] solutions did attempt mapping beyond LOS. However, they invariably require elaborate infrastructure with large antenna arrays, precisely calibrated setup, non real-time computation and extensive training if deep learning methods are involved. In most cases, the solutions are custom implemented using Software Defined Radios – e.g., phase synchronization across radio front-ends, bandwidth stitching to improve the resolution of the channel impulse response and so on. This makes it hard to adopt such solutions in existing commercial wireless chipsets. The other approach has been through extensive fingerprinting. In [40], Wi-Fi fingerprints from different devices are used to detect the adjacency of rooms and the hallway. The work requires significant amount of crowd-sourcing along with computational resources. In this context, note that mmWave radars (60GHZ, 77GHZ) are not suitable for penetrating building structures and hence do not offer anything additional when compared to traditional SLAM based techniques.

Radio Tomographic Imaging (RTI). RTI-based techniques [12], [25], [24] have been a useful alternative approach, particularly for its ability in mapping beyond LOS. However, existing literature primarily focuses on device-free (human) localization and target tracking [41] using a set of pre-calibrated, static and localized transceivers [26]. RTI is being recently explored as a mapping modality [42], [27], [24], [36], however almost all of the work requires a heavily calibrated setup. In [27], [43] an integrated solution is proposed using both LiDAR and RTI. The time-duration for data collection, along with the precise estimation of robot position at every instance, reduces the feasibility of real-world deployment. In [24], [36], experiments are carried out only inside a simulation environment that limits its extensibility to the real world.

Existing Research Gaps in RTI. As we discuss later, RTI attempts to solve an *ill-posed inverse problem* and the solution is extremely sensitive to the inputs to the problem (wireless measurements and sensor's location). Exisitng RTI literature primarily deals with noisy wireless measurements. Location uncertainty, a factor known to have a *multiplicative impact* [44] on the solution, has rarely been explored from a systems or empirical perspective. Also, to make such systems real-time and lightweight, it is vital to understand the computational aspects [45] of the RTI problem. In [46] compressed sensing is utilized to reconstruct the map by reducing the number of sample links, however the actual problem size remains same. Existing works addressing the computation aspects, focus mostly on target localization where a prior knowledge along with the node velocity is utilized to predict the node location inside the map [45]. Although it may reduce the computation cost for node localization, the application in the context of indoor mapping is negligible. In UBIQMAP, we identify such gaps and do the needful to address them.

3 BACKGROUND AND CHALLENGES

3.1 Radio Tomographic Imaging (RTI) Primer

Wireless signals get attenuated as they traverse along a medium and heavily so, as they pass through physical objects [17]. The extent of such attenuation depends on the length of path traversed by the signal and material properties (e.g., permittivity) of the traversing medium itself. RTI techniques estimate the spatial attenuation map or attenuation image, $X \in \mathbb{R}^N$, from a host of RF measurements performed across various locations in and around the Region of Interest (ROI), discretized into spatial blocks of dimension $\delta \times \delta$ sq.m.

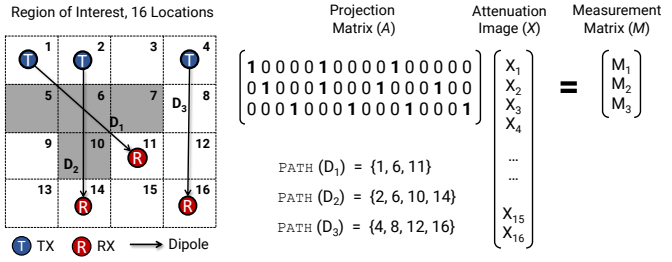

Fig. 2: Three dipoles, D_1, D_2 and D_3 are shown over the Region of Interest, along with their corresponding PATHs. The projection matrix $A_{3\times16}$ and the measurement matrix $M_{3\times1}$ are estimated from the dipoles. The task is to estimate the attenuation matrix or image X.

Assume a total of N discrete spatial indices or locations in X, where the attenuation coefficient at the n^{th} location is denoted by X_n. A measurement constitutes of estimating the total attenuation within a wireless link. We refer to such wireless links as *dipoles*. A dipole D_i is completely characterized by the transmitter location D_i^{TX}, the receiver location D_i^{RX} and the measured attenuation loss M_i. Let $\text{PATH}(D_i)$ be the set of locations traced by the Line-of-Sight (LOS) or straight line path connecting D_i^{TX} and D_i^{RX}. Essentially M_i can be (approximately) expressed as $\sum_n X_n$, such that, $n \in \text{PATH}(D_i)$. The approximation improves with increasing the spatial resolution of the grid cells. We express a system of measurements consisting of m dipoles, $D_1, D_2, \cdots, D_m$, in the linear form $AX = M$, where $X \in \mathbb{R}^N$ is the attenuation image, and $M \in \mathbb{R}^{m\times1}$ is the *measurement* matrix corresponding to m dipoles. $A \in \{0,1\}^{m\times N}$ denotes the binary *projection* matrix, where $A_{ij} = 1$, if $j \in \text{PATH}(D_i)$, otherwise $A_{ij} = 0$.

Ill-posed Inverse Problem. Note that, given A and X, it is relatively straightforward to estimate M, which we call the *forward* problem (see fig. 2). However, our task is to estimate X from A and M which is rather, an *inverse* problem. Given the presence of measurement noise in M, we can estimate X

by solving the following optimization problem in the least squares sense,

$$\widehat{X}_{ls} = \underset{X}{\operatorname{argmin}} ||AX - M||^2 \tag{1}$$

The solution to the above equation is equivalent to applying the *Moore-Penrose Pseudoinverse* on M, i.e., $\widehat{X} = (A^T A)^{-1} A^T M$. However, this requires A to be a full-rank matrix which is not valid in such a setting. This renders the problem *ill-posed* where the solution, $\widehat{X}$, varies drastically with slight changes in the input, M. To address such ill-posedness a regularization term is appended to eqn.(1), as follows.

$$\widehat{X}_{rls} = \underset{X}{\operatorname{argmin}} ||AX - M||^2 + \beta||X||^2 \tag{2}$$

This is referred to as the Tikhonov regularization method ($\beta > 0$ is a hyperparameter or weight value) and is a common tool for solving ill-posed inverse problems [47]. The generalized Tikhonov method uses a regularization operator L making the latter term $\beta||LX||^2$. In eqn.(2), L is the identity matrix operator. Note that such regularized inversion can still be conveniently expressed in the least square form as

$$\widehat{X} = ((A^T A + \beta\, L^T L)^{-1} A^T) M \tag{3}$$

Apart from Tikhonov regularization, techniques such as *Truncated Singular Value Decomposition* (TSVD) [12] or *Total Variation* (TV) [25] have been widely used in RTI literature. TSVD produces relatively noisy images due to the inclusion of high frequency components in the reconstructed image. TV is known to produce images with improved sharpness but suffers from an increased computational complexity relative to TSVD or Tikhonov. As a linear projection on the measurement data, Tikhonov is far more computationally lightweight (cf. TV) and is preferred for RTI systems that need frequent reconstruction updates. Further, we use the Tikhonnov regularization with L as the identity matrix operator as our performance baseline (TIKREG).

Attenuation Image Filtering. $\widehat{X}$ only represents the attenuation image and needs to be appropriately filtered to bytest approximate a binary occupancy map. The latter is required for various crucial applications including navigation and routing. Depending on the constraints, e.g., compute resource availability, time required and so on, such filtering can entail simple thresholding [48] to advanced de-noising techniques [49], [50].

The reconstruction quality, either the attenuation image or the filtered image, is measured using the *peak signal-to-noise ratio* (PSNR) metric [51], widely used in RTI literature. PSNR is computed by comparing the original map image and the filtered image. Specifically, it is expressed as the ratio of the maximum image pixel intensity value to noise in the logarithmic scale. Noise denotes the pixel wise mean square error (MSE) of the original and filtered image. For similar images, the MSE is relatively low making the PSNR high. It is denoted by the following formula,

$$PSNR = 20\, log_{10} \frac{\texttt{max\_intensity}}{MSE} \tag{4}$$

3.2 Challenges

While the majority of the existing RTI literature either focuses on theoretical analysis of reconstruction algorithms or simulation studies, very little attention has been paid to identifying the challenges that exist to adapt such techniques to end-to-end mobile systems. In the following, we highlight a couple of essential issues that seriously affect the reconstruction accuracy; however, they are insufficiently addressed in the research literature. Such issues are prevalent in any practical deployment of mobile systems targeted towards mapping indoor environments in challenging scenarios.

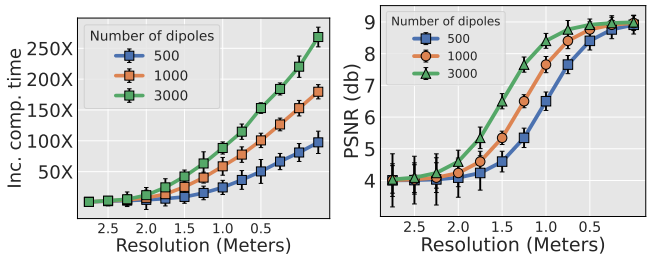

Fig. 3: Considering a baseline resolution of $\delta = 3\,m$, the *left* figure shows the increase in computation time with increasing resolution (lower values of δ). The figure on the *right* shows the corresponding PSNR values obtained.

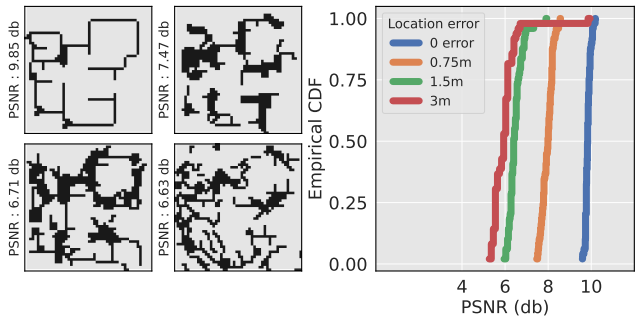

Fig. 4: Reconstructed figures for three different mean location error using TIKREG along with the CDF of the obtained PSNR.

Computational challenges Solving such ill-posed inverse problems require significant computational resources [45] and often incur high compute latency. Specifically, this reduces to solving a high dimensional optimization problem. Hence, a critical deployment challenge is to set up the dimensionality of the problem in a judicious way and modulo the hardware resources available. From eqn. (3), it is evident that the size of problem is governed by the dimension of the matrix $A \in \{0,1\}^{K \times N}$. The K rows in A denote individual measurements while the N columns represent the dimensionality of the solution or the resolution at which the attenuation image, $X \in \mathbb{R}^N$ is estimated. Arbitrarily increasing the resolution makes the computation prohibitively high without any appreciable increase in the reconstruction quality (diminishing returns). For instance, in fig. 3, there is no significant increase in PSNR beyond a resolution of $1\,\text{m} \times 1\,\text{m}$, however the computation cost keeps increasing. Second, it also hurts the overall reconstruction accuracy due to the inherent noise in the channel measurements. Thereby, a key strategy is to determine the spatial quantum, $\delta \times \delta$ at which the ROI is discretized. It is also equally important is to determine the set of measurements to use for the

solution. Each measurement, depending on the geometry of the dipole, captures information related to specific portions of the attenuation image. Hence, the larger the number *independent* dipoles (i.e., higher rank of A), the better the reconstruction accuracy.

Location uncertainty of transceivers Most works in the RTI literature that focus on solving the optimization problem stated in eqn.(3), consider a *noisy* measurement matrix, M, with a projection matrix, A, that is *noise free*. This is often the case where transceivers are statically deployed with their location information calibrated beforehand. Even in a couple of works that consider mobile transceivers [27], their location information is accurately estimated using highly orchestrated and precise robotic movements. As stated previously, none of these approaches promotes situations with imprecise location updates leading to erroneous estimation of the projection matrix. Unlike *RSS* noise, which is of *additive* nature, such location error is *multiplicative* and drastically impact the reconstruction accuracy. We demonstrate in fig. 4 that such errors, common in any wireless system, are critically coupled to the overall reconstruction accuracy.

4 System Design for UbiqMap

4.1 UbiqMap In a Nutshell

Mobility and dynamic deployment are the central crux of UbiqMap, making it unique concerning existing literature on RTI-based systems. We assume a setting where multiple mobile agents (e.g., first responders, robots) equipped with portable radios scout the RoI. These wireless transceivers, hereafter referred to as *nodes*, are necessarily a part of the agent's data communication system. We leverage these mobile nodes as a distributed sensing framework for our map estimation task. For UbiqMap, we consider Wi-Fi transceivers forming a mesh network. At its core, our system involves three primary functional components. First, a node topology estimation module that infers the relative locations of individual nodes over time. Second is a reconstruction module that implements the RTI algorithms for estimating the attenuation image, and third is a filtering module that estimates the structural map from the attenuation image.

4.2 Node Topology Estimation via Wireless Ranging

Unlike RTI systems that consider static nodes deployed at precisely known locations, UbiqMap continuously estimates the relative topology among the mobile nodes. The inter-nodal distance (*dipole length*) is estimated between a pair of nodes within the communication range. UbiqMap employs the Wi-Fi RTT or *Fine Time Measurement* protocol [21], [52] for the distance estimates. However, upcoming standards also support estimation of *Angle of Arrival* that makes location tracking even more robust [53], [54], [55]. The range estimates from each node are collected in a statically deployed *master node* that performs all the necessary computations for the topology estimation (as well as the eventual reconstruction). Additionally, the master node serves as the reference origin for UbiqMap's coordinate system.

Let $d_{i,j}$ denote the estimated range between $node_i$ and $node_j$ within a time interval Δt. Range entries for different node pairs pertaining to that interval are stored in the *Euclidean Distance Matrix* (EDM), $\mathbf{D^2}$ where $\mathbf{D^2}_{i,j} = d_{i,j}$. Δt is a tunable time interval adapted based on the temporal dynamics of the node topology. The topology is updated at the end of every Δt time slot, which we call *epoch*. We adopt the Classical Multidimensional Scaling (cMDS) [22] technique to estimate a 2D embedding of the node topology onto the physical space. The master node is treated as the origin of the embedded coordinate space.

Algorithm 1 Classical MDS based relative localization

Input: D^2
Output: X
1: Compute $\mathbf{G} = \frac{1}{2}\mathbf{H}\mathbf{D}^2\mathbf{H}$ where $\mathbf{H} = \mathbf{I} - \frac{1}{n}\mathbf{1}\,\mathbf{1}^T$
2: Find Eigen Value Decomposition of $\mathbf{G} = \mathbf{Q}\Lambda\mathbf{Q}^T$
3: $\mathbf{X} = \mathbf{Q}\sqrt{\Lambda}$

In this context, note that it is not necessary to obtain the inter-nodal ranges for every node pair for obtaining a correct topology estimate; a small fraction of all possible ranges is often sufficient to predict the rest (e.g., see OptSpace [56]). Second, cMDS estimates are sensitive to range noise, producing erroneous node topologies. We use a *stress* metric internally computed by the cMDS algorithm that estimates the goodness of fit between X and $\mathbf{X_{true}}$ [57]. We leverage this metric as an estimator of the localization error (see fig. 5), which is crucial for integrating the location uncertainty into UbiqMap's RTI solution.

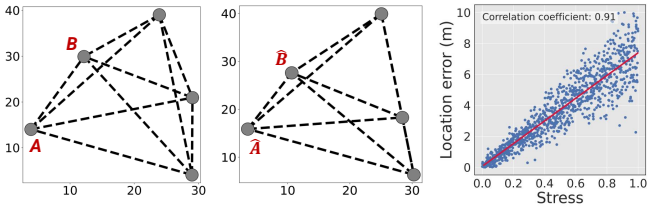

(a) Ground truth Topology (b) MDS Estimated Topology (c) Location Errors vs stress

Fig. 5: Estimated node topology from noisy range information. We also show the distribution of location errors incurred in individual nodes in the estimated topology for mean range errors from 1 m through 4 m.

Ranging Modality. In this paper, we contribute to the location uncertainty problem in RTI that remains independent of the choice of localization modality/technique. Our focus is primarily to demonstrate how UbiqMap embraces noisy location estimates common in an uncalibrated and ad-hoc setting. In fig. 6, we present the ranging error encountered by Wi-Fi FTM compared to Ultra Wideband (UWB) technology. UWB is known to be highly precise [58], [59] even in Non-Line-of-Sight (NLoS) conditions, where Wi-Fi FTM can suffer up to 2–5 m of ranging error. We purposefully choose Wi-Fi FTM to demonstrate the robustness of UbiqMap in the face of moderate localization errors. We still use a pre-calibrated deployment of UWB beacons to gather ground truth location estimates. We remind the reader that our goal in this paper is not using sophisticated location tracking modalities but rather demonstrate how UbiqMap is robust against location errors.

This article has been accepted for publication in IEEE Transactions on Mobile Computing. This is the author's version which has not been fully edited and content may change prior to final publication. Citation information: DOI 10.1109/TMC.2024.3442439

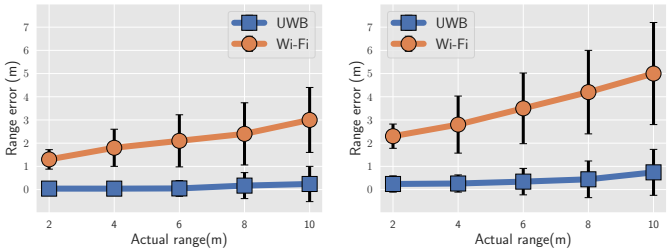

Fig. 6: Comparison of UWB and *FTM* ranges in LoS and NLoS conditions. The median range error for UWB is nearly negligible (≈ 30 cm) in both LoS and NLoS conditions w.r.t the ground truth, which makes it suitable to benchmark the *FTM* range error.

The movement of the nodes creates a diverse set of dipoles that scans various portions of the RoI covering both free space as well as areas with building structures. An edge within the estimated node topology represents a dipole if the corresponding node pair performs a channel measurement (wireless propagation loss) in the same epoch. The node topology is updated at the end of each epoch. The relatively slower movement of the nodes (≈1 m/s) compared to the range update rate (≈10 Hz), creates an opportunity to filter noisy topology estimates, thereby improving localization accuracy.

4.3 Efficient Reconstruction under Location Uncertainty

A mission critical system such as UbiqMap is intended to work in near real-time, continuously updating the underlying attenuation image, as the nodes move around the RoI. Two important performance indicators are the computational efficiency (e.g., latency) and accuracy of the reconstruction process. UbiqMap utilizes the GridFind algorithm to minimize the reconstruction latency by determining the optimal resolution at which the occupancy map is estimated. Second, it improves upon the state-of-the-art RTI methods to incorporate the uncertainty of the estimated node topology discussed previously.

■ **GridFind Algorithm.** A higher imaging resolution results in an improved reconstruction quality (e.g., higher PSNR); however, it suffers from an increased compute load. Fundamentally, the maximum resolution depends on the wavelength of the RTI signal (λ), e.g. ≈12 cm for Wi-Fi at the 2.4 GHz band. However, at this scale, the size of the resulting optimization problem (refer equation 3) is prohibitively high to be solved on an embedded class computer. For instance, it requires about 13K such 12 cm×12 cm 'pixels' to tile a 2000 sq.ft RoI.

The RoI is discretized at a spatial resolution of $\delta \times \delta$, where $\delta = K\lambda$, an integral multiple of the signal wavelength. The GridFind algorithm estimates the optimal value of K, i.e., K_{opt}, that maximizes the utility of the reconstruction process. Utility, in this context, is measured as the improvement in reconstruction quality with respect to the increase in computational cost. We demonstrate that $K < K_{opt}$ leads to diminishing returns, while for $K > K_{opt}$ the reconstruction quality deteriorates drastically.

Fig. 7 demonstrates the high-level intuition behind the GridFind (Algorithm 2). As evident in the setup $K = K_{high}$, measurements yielding from both LoS and NLoS scenarios are mapped to the same pair of grid cells. Given the already ill-posed nature of the problem, such inconsistencies severely degrade the quality of reconstruction. Without any prior knowledge of the structural map, we address this issue by identifying the simultaneous occurrence of LoS and NLoS measurements within individual grid cells for a given value of K. We represent the cell-specific measurements using a mixture model with one (either LoS or NLoS) or two (both LoS and NLoS) components. The *Akaike Information Criterion* (AIC) is used as the model predictor, a metric that gets minimized for choosing the most likely model parameter. We use the number of components in the mixture model as the parameter, that is assumed to be either one or two. GridFind algorithm defines a metric, $\Delta\,\mathrm{AIC} = \mathrm{AIC}(2) - \mathrm{AIC}(1)$. If LoS and NLoS scenarios coexist for a particular cell, i.e., the measurement pool has two observable RSS distributions, then $\mathrm{AIC}(2) \leq \mathrm{AIC}(1)$. On the other hand, if the measurements exclusively correspond to either LoS or NLoS, then $\mathrm{AIC}(1) \leq \mathrm{AIC}(2)$. Observe the change in $\Delta\,\mathrm{AIC}$ (in fig. 8) as a function of the spatial resolution, δ. Given the measurements, the GridFind algorithm searches for the maximum value of K, such that the majority (or a given percentage) of the grid cells exhibit a positive value of $\Delta\,\mathrm{AIC}$.

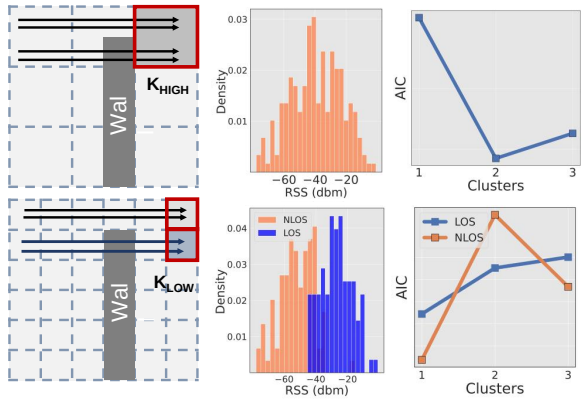

Fig. 7: Demonstation of how the AIC metric can be used to distinguish between distributions that are collected in pure LoS or NLoS versus that a mixture of LoS and NLoS observations.

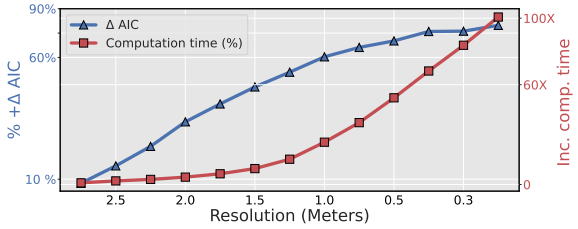

Fig. 8: An illustration of change in positive Δ AIC % with respect to resolution and the corresponding increase in computation time.

■ **Robust Tomographic Reconstruction.** In fig. 4, we highlight the sensitivity of the reconstruction process (eqn. 3) as a function of the localization accuracy of the dipoles. Even an average location error of 1–2 meters results in a PSNR deterioration of 3-4 dB, which renders the reconstructed map almost unusable.

Algorithm 2 GRIDFIND - Estimates optimal grid resolution

Input : ROI, DIPOLES (L_T, L_R, RSS_R), K_{max}, P_{max}
Output : K_{opt}

$K \leftarrow K_{max}$
while K ≥ 1 **do**
  Tile ROI into cells, C_i^K, each of dimension $K\lambda$
  Map all DIPOLES(L_T, L_R, RSS_R) $\leftarrow$ (C_T^K, C_R^K) such that, $L_T \subseteq C_T$ and $L_R \subseteq C_R$
  AICSET $\leftarrow \{\}$
  for all cell pairs (C_T^K, C_R^K) **do**
    Compute Δ AIC on $RSS(C_R^K)$
    Add Δ AIC to AICSET
  if percentage of +ve values in AICSET $\geq P_{max}$ **then**
    $K \leftarrow K_{opt}$
  else
    $K \leftarrow K - 1$
return K_{opt}

Recall that each row $A_i \in \{0,1\}^{1\times N}$ in the projection matrix $A \in \{0,1\}^{m\times N}$ represents the path traced by an observed (*noisy*) dipole. Let A and $\bar{A}$ be the observed and true projection matrices, respectively. A can be expressed as $\bar{A} + U$, where $U \in \{-1,0,1\}^{m\times N}$ is the uncertainty matrix that represents the noise in the A. In such a case, the L^2-norm minimization objective in equation 1 can be re-written as its *robust* counterpart as,

$$\begin{aligned}\widehat{X} &= \underset{X}{\operatorname{argmin}}\, \mathbf{E}||AX - M||^2 \\ &= \underset{X}{\operatorname{argmin}}\, \mathbf{E}||(\bar{A} + U)X - M||^2 \\ &= \underset{X}{\operatorname{argmin}}\, W^TW + 2W\mathbf{E}[U]X + X^T\mathbf{E}[U^TU]X \\ &\quad where, W = (\bar{A}X - M)\end{aligned} \tag{5}$$

For U being zero mean and uncorrelated, i.e., $\mathbf{E}[U] = 0$ and $\mathbf{E}[U^TU] = cI$ (for some constant $c > 0$), eqn. (5) reduces to the familiar Tikhonov regularization form (see eqn. 2) with a straightforward solution [44].

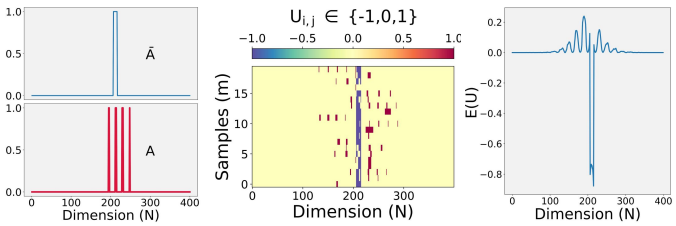

Fig. 9: (a) Projection ($\bar{A}$) of a sample dipole with its noisy observation in a grid of size 20×20, (b) Matrix $U \in \{-1,0,1\}^{\{30\times 400\}}$ for 30 noisy observations, and a non-zero E(U)(c)

However, we argue that the above assumption does not hold good in our system. In fig. 9, we showcase a single dipole $\bar{D}$ and a set of its noisy perturbations. Let D_i be an instance of that observation set, and j denote a location or a specific column in A. $U_{i,j} \in \{-1,0,1\}$ takes the value 0 at locations unaffected by the perturbation. $U_{i,j} = 1$, if $j \in$ PATH(D_i) and $j \notin$ PATH($\bar{D}$), similarly $U_{i,j} = -1$, if $j \notin$ PATH(D_i) and $j \in$ PATH($\bar{D}$). It is evident that, $\mathbf{E}(U_{i,j}) \geq 0$ for $j \notin$ PATH($\bar{D}$) and $\mathbf{E}(U_{i,j}) \leq 0$ for $j \in$ PATH($\bar{D}$) (also demonstrated in fig. 9).

■ **Stochastic approximation.** Assuming a non-zero $\mathbf{E}(U)$, we resort to a stochastic approximation of the dipole that makes the solution computationally simple and effective in improving the reconstruction accuracy. In the standard RTI formulation, $A_{i,j} = 1$ iff $j \in$ PATH(D_i), zero otherwise. Instead of such *hard* assignment, for every location L, we assign a likelihood value $P(A_{i,L} = 1 \,|\, \text{PATH}(D_i))$, for each dipole D_i. Intuitively, if $j \in$ PATH(D_i), instead of assigning the entire likelihood to a single location j, we distribute the same among the locations in the *neighbourhood* of j. The likelihood value signifies the contribution of the particular location in the observed attenuation measurement of the dipole in question. Ofcourse, the radius of such neighbourhood depends on the average localization error.

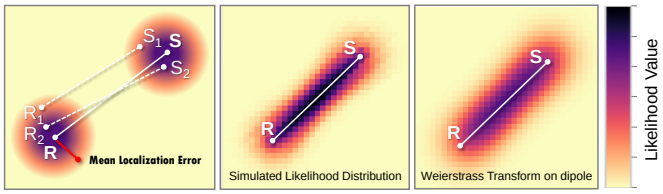

Fig. 10: An illustration of different dipole configurations possible for a given mean location error along with their maximum likelihood mass and stochastic approximation.

In fig. 10, we simulate an observed dipole RS along with many probable instances of the corresponding original dipole $\overline{RS}$ (e.g., R_1S_1, R_2S_2) assuming an average localization error. The superimposed instances highlight how the likelihood mass is distributed among its neighbourhood instead of being contained strictly along RS. To approximate the distributed likelihood mass, we use the *Weierstrass transform* [60], [61] on the observed dipole, which is equivalent to convolving the latter with a Gaussian filter kernel. We use a two-dimensional Gaussian kernel with a standard deviation equal to the mean location error. Recall that the *stress value* from the CMDS algorithm is a fairly good predictor of the localization error (see, fig. 5). UBIQMAP applies such transformation to each observed dipole in A to create the stochastically approximated version A_{STOC}. We set up the reconstruction problem as (β and L being the hyperparameter and the Tikhonov operator respectively),

$$\widehat{X}_{stoc} = \underset{X}{\operatorname{argmin}}\, ||A_{\text{STOC}}X - M||^2 + \beta||LX||^2 \tag{6}$$

■ **Choice of Tikhonov operator.** It is well understood that the Tikhonov operator (L) can modulate certain desirable properties in the attenuation image, for instance, overall smoothness, sharpness etc. Two commonly used operators in RTI literature are the Identity matrix [12], [62] and the Difference [25] operators. However, their performance is quite limited, particularly in the face of location noise (see fig. 11 for a comparison). A key observation in our context is that building structures have continuous and sharp boundaries with the surrounding free space, resulting in prominent *edges* in the attenuation image. We employ the *Laplacian operator*, which is expressed as the sum of second-order partial derivatives of the intensities (attenuation coefficients) along the horizontal and vertical directions. Note that, the Laplacian operator is extremely sensitive random noise spikes, hence X needs to be smoothed first. A common

practice (e.g., in image processing) is to use a composition of the Laplacian and a Gaussian smoothing kernel that makes the edge detector robust against noise. We use a *Laplacian of Gaussian* kernel [63] of size 5×5.

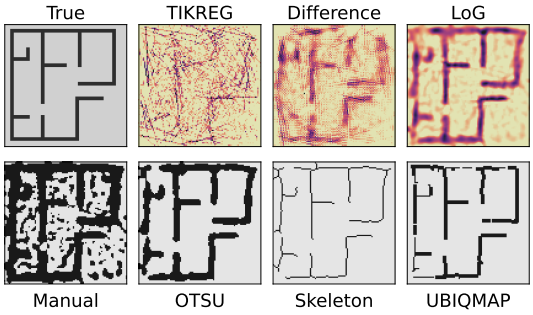

Fig. 11: Reconstructed attenuation maps for different regularization operators along with the thresholded *LoG* attenuation map for different threshold functions.

4.4 Attenuation Image to Obstacle Map

Although the attenuation image gives a perceptual notion of the obstacle map, further refinement is critical for many applications. Take, for instance, the task of creating navigation routes within the map for robots or indoor drones. A binary map is often useful for such applications that is solely meant for distinguishing free space from obstacles. A natural choice is using a specific attenuation value for manual thresholding. However, the noise in the resulting obstacle map is susceptible to the chosen threshold value.

We use a thresholding scheme called the OTSU's method [49], where the pixels are mapped to a bimodal class while reducing the intraclass distance. However, OTSU estimates a global threshold that disregards spatial correlation [64]. For instance, building structures are more likely to be contiguous and not speckles that are randomly scattered around. We use a morphological transform called *skeletonization* on the OTSU thresholded image that preserves the topological patterns and estimates a single pixel-wide medial axis of the structures. We enhance it further by dividing the skeleton into a set of connected components and growing each component to a specific width. The width depends on OTSU thresholded width of the structure for a particular component.

5 Prototype Implementation and Evaluation

For evaluation, we build a portable system prototype with four headmounted mobile nodes and a single, randomly deployed static node. The system can be deployed quickly without requiring any additional infrastructure support or calibration.

5.1 Implementation Details

As shown in fig. 12 (*left*), each UBIQMAP node consists of two Wi-Fi integrated low-power, single-core microcontroller SOC units (ESP32-S2 [65]) mounted on two sides of the helmet. We use two transceivers primarily to avoid body blocking effects in the LOS path and to provide some redundancy in measurements. Although such an arrangement proved practical for our proof-of-concept device, a productized version will have a more sophisticated antenna layout, potentially integrated with the helmet. A fraction of the nodes (≈50%), configured as transmit nodes continuously broadcast beacon packets at an approximate rate of 10 Hz. Such nodes are also configured as *FTM responders* that respond to FTM requests sent by the client nodes, which act as *FTM initiators*. Thereby, such client nodes estimate their distances to the responder nodes. ESP32-S2 SOC natively supports the 802.11mc Wi-Fi RTT or FTM ranging protocol. The clients record *RSS* measurements for individual transmit nodes, along with their inter-nodal distance information. Additionally, every client is also equipped with a Ultra-wideband (UWB) ranging module (Qorvo MDEK1001 [66]) that estimates its distances to statically deployed and pre-localized UWB anchors (tripods in fig. 12) at a sub-decimeter level accuracy. The UWB measurements solely serve as a means to estimate the *groundtruth location information and are not used for the RTI solution.* For both Wi-Fi, apart from FTM ranges, we use the onboard inertial sensors to improve localization accuracy. We fuse the noisy range estimates (fig. 13) along with the inertial sensor data using the popular Extended Kalman Filter (EKF) heuristic [67].

While the above mentioned nodes are used towards sensing and are typically mobile, UBIQMAP uses a central node that is *static* (but randomly deployed) and slightly more resourceful than the microcontroller units. Note that the static node only marks the map coordinate's origin, and its random placement does not affect the overall quality of the map reconstruction. We use a RaspberryPi-4 Model B (with 4GB memory) as the central node that interfaces with a ESP32-S2 unit for ranging with the mobile nodes. All measurements (*RSS* and inter-nodal ranges) from the sensing network are collated in the central node. It runs two processes in real-time: (i) the CMDS algorithm to estimate the dynamic node topology, and (ii) the UBIQMAP RTI reconstruction procedure with the new set of dipoles obtained after each topology estimation. Depending on the ROI size and GRIDFIND estimated resolution, we update the maps at a rate of 0.5–2 Hz with a reasonable PSNR at a steady state.

Additionally, we deploy a 0X-DELTA [68] robot equipped with a SICK LMS111-10100 [69] 2D LiDAR module (see fig. 16) to generate a SLAM based reconstruction of the region of interest. Both the robot and LiDAR are suitable for outdoor usage such that it can be used to go around the periphery of the building to map its contour (see fig. 17). The robot is equipped with an NVIDIA JETSON NANO module that provides ample computing power to run SLAM algorithms. We use the open-sourced `lidarslam_ros2` package provided by the ROS software platform [70] that runs on our robot.

5.2 Deployment Scenarios

We deploy UBIQMAP in two real scenarios: (i) a large building foyer area (≈3000 sq. ft) with a relatively simple structural layout, and (ii) a residential apartment (indoor area ≈800sq.ft) with a considerably complex layout – see fig. 12 for layout details. While the foyer area only has four large pillars, each of width $2\,\text{m}\times2\,\text{m}$, the apartment has four large rooms with brick walls of various shapes and sizes and three inaccessible areas (shut doors). Additionally, note the materials marked in fig. 12: a drywall (yellow block),

This article has been accepted for publication in IEEE Transactions on Mobile Computing. This is the author's version which has not been fully edited and content may change prior to final publication. Citation information: DOI 10.1109/TMC.2024.3442439

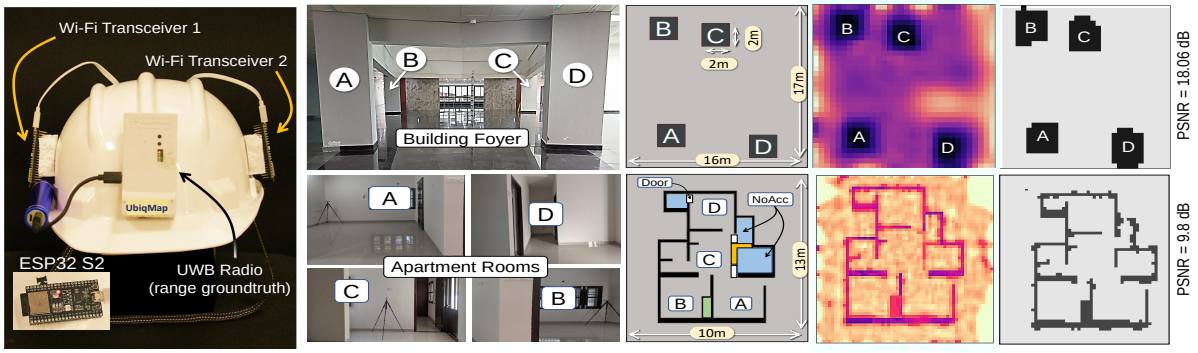

Fig. 12: (left) UBIQMAP mobile node prototype. The remaining figures show the layout of the deployment scenarios and the subsequently reconstructed attenuation/obstacle maps. In the apartment, three zones marked as NOACC are deliberately made inaccessible with doors shut. Materials marked in the apartment: dry wall (yellow block), three closed wooden doors with glass panes (white blocks) and a wall-finished wardrobe with metallic parts (green block).

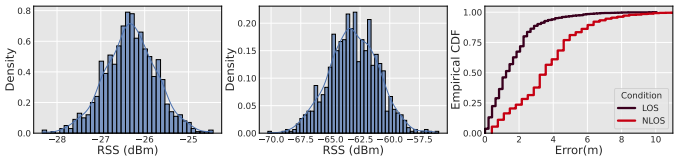

Fig. 13: Fluctuation in *RSS* measurements due to random fading in LOS (3–4dB) and NLOS (8–10dB) scenarios. The median location error is ≈2 m in LOS and ≈ 3.5 m in NLOS conditions.

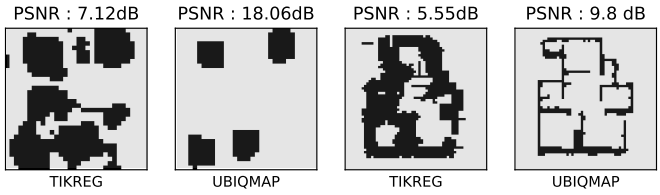

Fig. 14: For an average location error of 2–3 m, note that how the stochastic approximation of the dipoles in UBIQMAP help achieve high quality reconstructions compared to the baseline TIKREG bench marked on the same measurement set.

three closed wooden doors with glass panes (white blocks) and a wall-finished wardrobe (green block) with metallic parts. The non-accessible regions are marked NOACC (blue). In both scenarios, we use four volunteers (along with the static control node) who walk randomly within and around the mentioned areas at an approximate speed of 1 m/sec. For the building foyer area, we collect measurement traces worth of ≈4 minutes resulting in about $8K$ dipoles. The apartment being located on the ground floor, we collect measurements both indoors as well as outdoors. Overall, we collect ≈6 minutes worth of measurements resulting in a little over $9K$ dipoles (we had many missing ranges in this case). Note that in our real-time setup, a clearly interpretable reconstruction is achieved way earlier than the total trace collection time. Additional measurement traces are used for systematic performance evaluation.

5.3 Testbed Results

We achieve reasonable reconstruction quality for both – the more straightforward foyer area (18 dB+ in about 20 seconds at resolution 5λ i.e., 0.6 m) as well as for the complex apartment layout (9 dB in about 50 seconds at resolution 3λ i.e., 0.36 m). Fig. 13 showcases the noise associated with the obtained *RSS* and the estimated locations. Fig. 14 demonstrates preliminary results to showcase how UBIQMAP outperforms the baseline with similar measurement efforts.

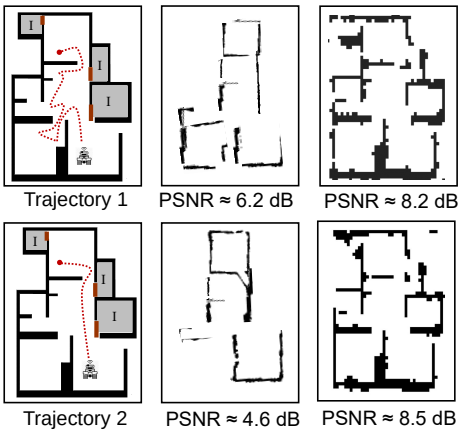

Fig. 15: Comparison of SLAM-based map for a different predefined trajectory with UBIQMAP generated map for random trajectories. A slight change in the robot trajectory hugely decreases the SLAM's accuracy in contrast to the UBIQMAP, which remains nearly unaffected by the trajectory choice.

UBIQMAP versus SLAM. We demonstrate the effectiveness of UBIQMAP compared to SLAM in mapping enclosed indoor spaces or areas that are sparingly accessible. First, in fig. 15, we show how SLAM-based maps are extremely sensitive to minor variations in the scanning trajectory, unlike their RTI-based counterparts. This is particularly true for shorter trajectories - observe a 2 dB degradation in PSNR between trajectories 1 and 2. For UBIQMAP, the reconstruction is way more robust, obviating the need for sophisticated trajectory planning.

Second, unlike SLAM, a key feature of an RTI system lies in its ability to map spaces beyond LOS. In fig. 16, we show how the reconstruction quality for SLAM is tightly coupled to the accessibility of the indoor space. UBIQMAP performs much better overall, even where no or very little indoor access is provided. Third, fig. 17 demonstrates an extreme situation where we restrict ourselves to dipoles collected

This article has been accepted for publication in IEEE Transactions on Mobile Computing. This is the author's version which has not been fully edited and content may change prior to final publication. Citation information: DOI 10.1109/TMC.2024.3442439

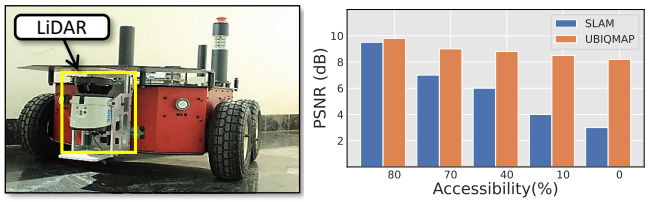

Fig. 16: (*Left*) 0X-DELTA robot equipped with 2D LiDAR. (*Right*) Performance analysis of UBIQMAP with SLAM for diminishing accessible region.

only in the outdoor area, i.e., with *zero*-access indoors. The four paths through which the volunteers moved during data collections are marked with dotted lines. UBIQMAP reconstructs the obstacle map reasonably well (PSNR 8.2 dB). Overall, we achieve nearly 30% better reconstruction accuracy by UBIQMAP as compared to SLAM.

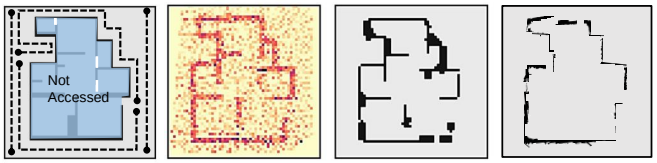

Fig. 17: Reconstructed attenuation and obstacle map by UBIQMAP as compared to SLAM for *zero* access to the apartment indoors.

Mapping beyond building structures. Besides adeptly mapping structural entities of the building, UBIQMAP can be leveraged to depict entities such as furniture, humans etc. Such functionalities are essential in tactical scenarios where detecting human presence in enclosed spaces is crucial. We demonstrate two specific instances where (i) we place a large-sized wooden shelf in the middle of one room and (ii) a couple of human volunteers stand in another room together (see fig. 18). Observe the corresponding attenuation maps that clearly reflect their presence. Although such entities are evident within the attenuation map, it should be noted that such details cannot be easily filtered out by simple techniques (e.g., OTSU's method). For such application specific filtering we often need non-trivial image segmentation algorithms [71], [72] depending on the type of entity we want to look out for. Our primary contribution is to unveil the attenuation map, in a pervasive setting, that can be fed to such algorithms (designing them is beyond the scope of this paper).

Material identification. We leverage UBIQMAP's attenuation image to predict the material properties of structures present on the obstacle map. In fig. 19 we showcase the relative attenuation coefficients estimated for various parts of the building structure - an information that is not available from SLAM-based mapping. We observe that the material identification accuracy can be improved using a higher resolution and significantly more measurements, which hampers real-time computation. Currently UBIQMAP's algorithms are fine tuned to estimate structural maps and its material identification capabilities are limited. Our current observations on inferencing material types are

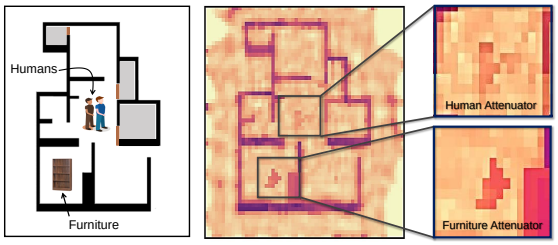

Fig. 18: UBIQMAP captures the presence of the furniture (wooden shelf) along with the human beings within the attenuation map.

predominantly qualitative. We intend to carry out a rigorous quantitative analysis as a future work.

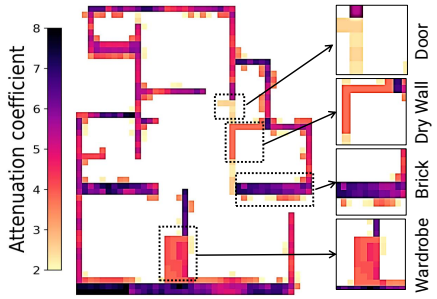

Fig. 19: Potential use of UBIQMAP to predict materials properties of structures in an attenuation image. Attenuation profiles of various materials are typically pre-calibrated.

UWB versus FTM based reconstruction. By utilizing UWB ranging for localization, we achieve a PSNR $\approx$ 8.5 dB with only 25% exploration, unlike Wi-Fi ranging based localization that requires at least 35–40% exploration to reach a similar level of PSNR. With increase in exploration of ROI the reconstruction accuracy of both UWB and Wi-Fi becomes practically the same (see fig. 20). We demonstrate how UBIQMAP can deal with noisy location data that has a multiplicative effect on the reconstruction accuracy (unlike *RSS* noise that has an additive effect).

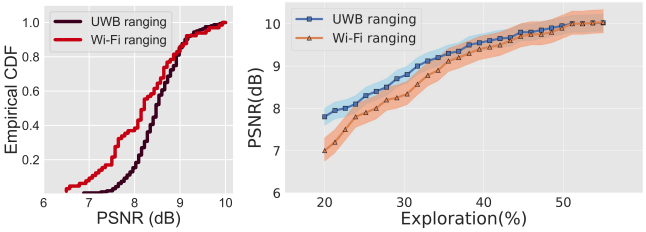

Fig. 20: UBIQMAP embraces Wi-Fi ranging, a relatively less accurate modality for localization, to achieve similar levels of reconstruction accuracy as compared to its highly accurate counterpart - Ultra Wideband (UWB) based ranging.

6 SCALED-UP STUDIES

In the previous section, we evaluate the performance of UBIQMAP in real world scenarios. To further our insights on its performance, we perform scaled-up simulation studies in controlled settings. Such simulations help us tune various control knobs to understand the RTI performance better, for instance - ROI size, layout complexity, number of dipoles, the speed at which the mobile nodes move, localization error and so on.

Simulated floor plans. We simulate two floor areas of size 1230 sq.ft and 2500 sq.ft referred as *Map 1* and *Map 2* respectively (see fig. 21). Our primary objective is to bolster the results obtained in the apartment (previous section) with additional layout maps and derive more insights.

6.1 Performance Evaluation and Insights

Grid resolution. We demonstrate the effect of choosing an optimal grid resolution as opposed to the *best* possible resolution. In fig. 21, we show that for a resolution of $\delta = 0.8\,m$, we obtain PSNRs equal to 9.29 dB and 8.61 dB respectively for *Map 1* and *Map 2*. Further decreasing δ shoots up the computation cost without appreciable gains in PSNR metric.

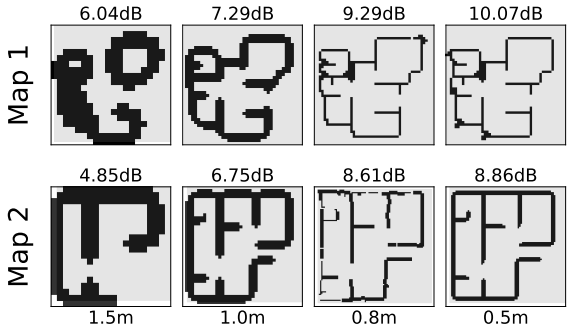

Fig. 21: An illustration of change in PSNR with respect to resolution. As can be seen after the optimal resolution there is no significant change in the PSNR value.

Location noise and choice of parameter. A significant challenge of *in-the-wild* deployment of an RTI system lies in appropriate prediction and treatment of location noise, which is known to have a multiplicative effect unlike *RSS* noise. As discussed earlier, the stochastic approximation using Weierstrass transform can effectively reduce its effect, however choice of the parameter σ plays an important role. Studies [73] show the impact of Weierstrass transform maximizes for the mean error and degrades for other choices. We show (in fig. 22) how the PSNR is maximized for σ equal to the mean location error. Other choices of σ lead to sub-optimal improvement.

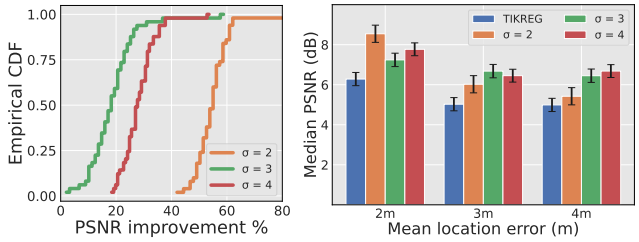

Fig. 22: CDF of percentage PSNR improvement over TIKREG for a mean location error of 2 m. The bar graphs show how the overall PSNR is impacted by the choice of σ for a given location error.

Number of nodes and average velocity. In the previous section, we are limited to four mobile nodes with an approximate node velocity of 1m/sec. However, the simulation allows us to experiment with various number of nodes and their corresponding velocities. More importantly, this allows us to experiment with various trajectories that the nodes follow while sensing. In fig. 23 we show the improvement

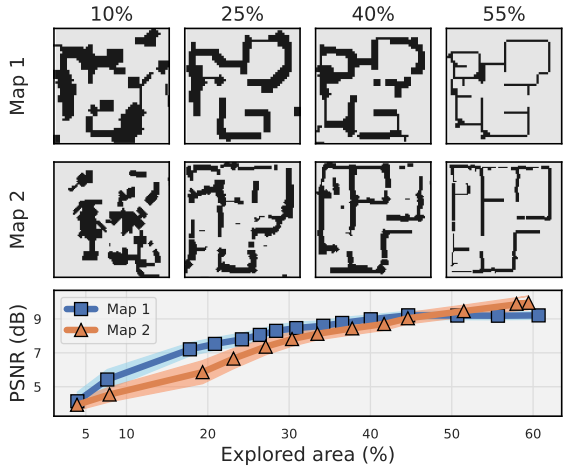

Fig. 23: An illustration of increase in accuracy with respect to increase in explored area. As can be seen, within 40 percent area exploration UBIQMAP can produce a highly accurate image of the original map.

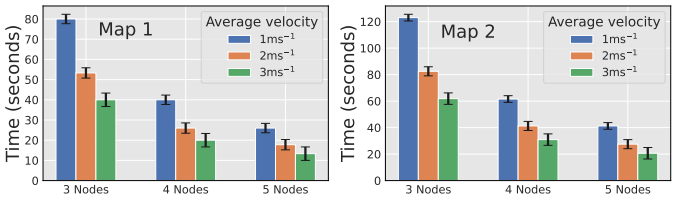

Fig. 24: UBIQMAP performance evaluation with different number of mobile nodes and their average velocity. We have shown the minimum time required by UBIQMAP in different setups to map an indoor environment with an PSNR above 8dB.

in the reconstruction quality as a function of the percentage exploration of the ROI. It is remarkable that in both the cases an exploration of ≈40% leads to a PSNR of 8 dB+. Compare such results with SLAM-based exploration techniques that need explicit exploration in all LOS reachable zone. We also experiment with various node velocities along with the number of nodes to understand the potential of UBIQMAP in time-critical missions as shown in fig. 24.

■ **Additional Remarks and Limitations.** UBIQMAP does not have any direct way to detect heavy multipath fading that can severely impact FTM ranging as well as *RSS* noise. Environmental factors such as temperature fluctuations and weather conditions [74] also impact the *RSS* and *FTM* values. Although we show UBIQMAP performance in ambient conditions, its resilience in adverse climatic conditions must be thoroughly evaluated. Existing literature explores the Wi-Fi Channel State Information (CSI) to create inference models for predicting heavy multipath or give better insights for range correction [75], [21]. We separately explore the idea of utilizing CSI to improve the accuracy of UBIQMAP. However, we find the inference models over-fit too easily and cannot be applied across different ROI sites. Second, it also increases the computation significantly, hence not justifiable in our current setup. Deep learning approaches [76] show near accurate prediction of *RSS* for a given location without being physically present. The future direction of work could be to utilize such techniques for indoor mapping in situations where the deployment of mobile devices is restrictive or not feasible.

7 Conclusion

In this paper, we propose UbiqMap, an end-to-end prototype that can reconstruct an indoor environment without any dependency on pre-deployed infrastructure. We discuss the effect of location noise on the reconstruction quality and propose strategies to reduce the same. Second, we also thoroughly analyze the computation cost involved with such reconstruction. We implement a UbiqMap prototype and deploy it in two real environments along with a couple of simulated ones. UbiqMap outperforms the baseline RTI algorithm by nearly 30% to 40% in terms of map reconstruction quality. Additionally, we show the capabilities of UbiqMap to reconstruct totally inaccessible regions along with differentiating between material properties of the obstacles. UbiqMap takes the state-of-the-art RTI systems a step closer to real-world deployment, particularly in dynamic environments.

References

[1] U. M. Khan, R. H. Venkatnarayan, and M. Shahzad, "RFMap: Generating indoor maps using RF signals," in *Proc. of IEEE IPSN 2020*.

[2] E. Dong, J. Xu, C. Wu, Y. Liu, and Z. Yang, "Pair-navi: Peer-to-peer indoor navigation with mobile visual SLAM," in *in Proc. of IEEE INFOCOM 2019*.

[3] C. X. Lu, S. Rosa, P. Zhao, B. Wang, C. Chen, J. A. Stankovic, N. Trigoni, and A. Markham, "See through smoke: robust indoor mapping with low-cost mmwave radar," in *Proc. of ACM MOBICOM 2020*.

[4] X. Deng, Z. Zhang, A. Sintov, J. Huang, and T. Bretl, "Feature-constrained active visual SLAM for mobile robot navigation," in *Proc. of ICRA 2018*.

[5] A. Arun, R. Ayyalasomayajula, W. Hunter, and D. Bharadia, "P2SLAM: Bearing based Wi-Fi SLAM for indoor robots," *IEEE Robotics and Automation Letters*, vol. 7, no. 2, pp. 3326–3333, 2022.

[6] NIST, "PSCR usability results tool:voices of first responders," *NIST PSCR*, 2023. [Online]. Available: https://publicsafety.nist.gov/analyzer.html

[7] X. Du, X. Liao, M. Liu, and Z. Gao, "CRCLoc: A crowdsourcing-based radio map construction method for Wi-Fi fingerprinting localization," *IEEE Internet of Things Journal*, vol. 9, no. 14, pp. 12 364–12 377, 2021.

[8] W. Li, X. Xu, Y. Wang, and D. Li, "A survey of crowdsourcing-based indoor map learning methods using smartphones," *Results in Control and Optimization*, vol. 10, p. 100186, 2023.

[9] H. Choset and K. Nagatani, "Topological simultaneous localization and mapping (slam): toward exact localization without explicit localization," *IEEE Transactions on Robotics and Automation*, vol. 17, no. 2, pp. 125–137, 2001.

[10] K. Chen, J. P. de Vicente, G. Sepulveda, F. Xia, A. Soto, M. Vazquez, and S. Savarese, "A behavioral approach to visual navigation with graph localization networks," in *Proc. of Robotics: Science and Systems*, 2019.

[11] D. S. Chaplot, R. Salakhutdinov, A. Gupta, and S. Gupta, "Neural topological slam for visual navigation," in *Proc. of IEEE/CVF International Conference on Computer Vision 2020*.

[12] J. Wilson and N. Patwari, "Radio tomographic imaging with wireless networks," *IEEE Transactions on Mobile Computing*, vol. 9, no. 5, pp. 621–632, 2010.

[13] F. Adib and D. Katabi, "See through walls with Wi-Fi!" in *Proc. of ACM SIGCOMM 2013*.

[14] M. Zhao, Y. Liu, A. Raghu, T. Li, H. Zhao, A. Torralba, and D. Katabi, "Through-wall human mesh recovery using radio signals," in *Proc. of IEEE/CVF International Conference on Computer Vision 2019*.

[15] D. Lee, D. Berberidis, and G. B. Giannakis, "Adaptive bayesian radio tomography," *IEEE Transactions on Signal Processing*, vol. 67, no. 8, pp. 1964–1977, 2019.

[16] H. Hashemi, "The indoor radio propagation channel," *in Proc. of IEEE*, vol. 81, no. 7, pp. 943–968, 1993.

[17] T. S. Rappaport, "Rappaport wireless communications," 1996.

[18] N. Antunes, V. Pipiras, and G. Jacinto, "Regularized inversion of flow size distribution," in *Proc. of IEEE INFOCOM 2019*.

[19] V. K. Ivanov, V. V. Vasin, and V. P. Tanana, *Theory of linear ill-posed problems and its applications*. Walter de Gruyter, 2013, vol. 36.

[20] A. Mishra, U. K. Sahoo, and S. Maiti, "Robust radio tomographic imaging for localization of targets under uncertain sensor location scenario," *Digital Signal Processing*, vol. 137, p. 104030, 2023.

[21] K. Jiokeng, G. Jakllari, A. Tchana, and A.-L. Beylot, "When FTM discovered MUSIC: Accurate Wi-Fi-based ranging in the presence of multipath," in *Proc. of IEEE INFOCOM 2020*.

[22] N. Saeed, H. Nam, T. Y. Al-Naffouri, and M.-S. Alouini, "A state-of-the-art survey on multidimensional scaling-based localization techniques," *IEEE Communications Surveys & Tutorials*, vol. 21, no. 4, 2019.

[23] B. Wei, A. Varshney, N. Patwari, W. Hu, and T. Voigt, "DRTI: Directional radio tomographic imaging," in *Proc. of IEEE IPSN 2015*.

[24] T. Matsuda, Y. Nishikawa, E. Takahashi, T. Onishi, and T. Takeuchi, "Binary Radio Tomographic Imaging in Factory Environments Based on LoS/NLoS Identification," *IEEE Access*, vol. 11, 2023.

[25] J. Wilson, N. Patwari, and F. G. Vasquez, "Regularization methods for radio tomographic imaging," in *2009 Virginia Tech Symposium on Wireless Personal Communications*.

[26] Q. Guo, Y. Li, X. Liang, J. Dong, and R. Cheng, "Through-the-wall image reconstruction via reweighted total variation and prior information in radio tomographic imaging," *IEEE Access*, vol. 8, 2020.

[27] A. Gonzalez-Ruiz, A. Ghaffarkhah, and Y. Mostofi, "An integrated framework for obstacle mapping with see-through capabilities using laser and wireless channel measurements," *IEEE Sensors Journal*, vol. 14, no. 1, pp. 25–38, 2013.

[28] K. Khoshelham and S. O. Elberink, "Accuracy and resolution of kinect depth data for indoor mapping applications," *In Sensors*, vol. 12, no. 2, pp. 1437–1454, 2012.

[29] H. Surmann, A. Nüchter, and J. Hertzberg, "An autonomous mobile robot with a 3D laser range finder for 3D exploration and digitalization of indoor environments," *Robotics and Autonomous Systems*, vol. 45, no. 3-4, pp. 181–198, 2003.

[30] R. Gao, M. Zhao, T. Ye, F. Ye, Y. Wang, K. Bian, T. Wang, and X. Li, "Jigsaw: Indoor floor plan reconstruction via mobile crowdsensing," in *Proc. of ACM MOBICOM 2014*.

[31] S. Pradhan, G. Baig, W. Mao, L. Qiu, G. Chen, and B. Yang, "Smartphone-based acoustic indoor space mapping," *in Proc. of IMWUT 2018*.

[32] B. Zhou, M. Elbadry, R. Gao, and F. Ye, "Batmapper: Acoustic sensing based indoor floor plan construction using smartphones," in *Proc. of ACM MOBICOM 2017*.

[33] Z. Yang and R. R. Choudhury, "Maplearn: Indoor mapping using audio," 2023. [Online]. Available: https://openreview.net/pdf?id=PdwrCm5Msr

[34] M. Alzantot and M. Youssef, "Crowdinside: Automatic construction of indoor floorplans," in *Proceedings of the 20th International Conference on Advances in Geographic Information Systems*, 2012, pp. 99–108.

[35] G. Zhu, C. Wu, B. Wang, and K. R. Liu, "Floor plan reconstruction with high-precision RF-based tracking," in *Proc. of IEEE ICASSP 2022*.

[36] S. Depatla, L. Buckland, and Y. Mostofi, "X-ray vision with only Wi-Fi power measurements using rytov wave models," *IEEE Transactions on Vehicular Technology*, vol. 64, no. 4, pp. 1376–1387, 2015.

[37] Y. Wang, Z. Zhou, and K. Wu, "Sensor-free corner shape detection by wireless networks," in *Proc. of IEEE ICPADS 2014*.

[38] A. Pallaprolu, B. Korany, and Y. Mostofi, "Wiffract: a new foundation for RF imaging via edge tracing," in *Proc. of MOBICOM 2022*.

[39] B. Korany and Y. Mostofi, "Counting a stationary crowd using off-the-shelf Wi-Fi," in *Proc. of ACM MOBISYS 2021*.

[40] Y. Jiang, Y. Xiang, X. Pan, K. Li, Q. Lv, R. P. Dick, L. Shang, and M. Hannigan, "Hallway based automatic indoor floorplan construction using room fingerprints," in *Proc. of UBICOMP 2013*.

[41] N. Patwari and J. Wilson, "RF sensor networks for device-free localization: Measurements, models, and algorithms," *in Proc. of IEEE*, vol. 98, no. 11, pp. 1961–1973, 2010.

[42] C. R. Karanam and Y. Mostofi, "3D through-wall imaging with unmanned aerial vehicles using Wi-Fi," in *Proc. of IEEE IPSN 2017*.

[43] A. Gonzalez-Ruiz and Y. Mostofi, "Cooperative robotic structure mapping using wireless measurements—a comparison of random and coordinated sampling patterns," *IEEE Sensors Journal*, vol. 13, no. 7, pp. 2571–2580, 2013.

[44] S. P. Boyd and L. Vandenberghe, *Convex optimization*. Cambridge university press, 2004.

[45] J. Wang, Q. Gao, P. Cheng, Y. Yu, K. Xin, and H. Wang, "Lightweight robust device-free localization in wireless networks," *IEEE Transactions on Industrial Electronics*, vol. 61, no. 10, pp. 5681–5689, 2014.

[46] M. A. Kanso and M. G. Rabbat, "Compressed RF tomography for wireless sensor networks: Centralized and decentralized approaches," in *International Conference on Distributed Computing in Sensor Systems*. Springer, 2009, pp. 173–186.

[47] C. R. Vogel, *Computational methods for inverse problems*. SIAM, 2002.

[48] P. K. Sahoo, S. Soltani, and A. K. Wong, "A survey of thresholding techniques," *Computer Vision, Graphics, and Image Processing*, vol. 41, no. 2, pp. 233–260, 1988.

[49] N. Otsu, "A threshold selection method from gray-level histograms," *IEEE Transactions on Systems, Man, and Cybernetics*, vol. 9, no. 1, pp. 62–66, 1979.

[50] P. K. Saha, G. Borgefors, and G. S. di Baja, "A survey on skeletonization algorithms and their applications," *Pattern recognition letters*, vol. 76, pp. 3–12, 2016.

[51] A. Hore and D. Ziou, "Image quality metrics: PSNR vs. SSIM," in *Proc. of International Conference on Pattern Recognition 2010*.

[52] M. Ibrahim, H. Liu, M. Jawahar, V. Nguyen, M. Gruteser, R. Howard, B. Yu, and F. Bai, "Verification: Accuracy evaluation of Wi-Fi fine time measurements on an open platform," in *Proc. of ACM MOBICOM 2018*.

[53] J. Shenoy, Z. Liu, B. Tao, Z. Kabelac, and D. Vasisht, "RF-protect: privacy against device-free human tracking," in *Proc. of ACM SIGCOMM 2022*.

[54] F. Adib, Z. Kabelac, D. Katabi, and R. C. Miller, "3D tracking via body radio reflections," in *Proc. of NSDI 2014*.

[55] S. Wang, X. Jiang, and H. Wymeersch, "Cooperative localization in wireless sensor networks with AoA measurements," *IEEE Transactions on Wireless Communications*, vol. 21, no. 8, pp. 6760–6773, 2022.

[56] R. H. Keshavan, A. Montanari, and S. Oh, "Matrix completion from a few entries," *IEEE Transactions on Information Theory*, vol. 56, no. 6, pp. 2980–2998, 2010.

[57] D. Jia, W. Li, P. Wang, X. Feng, H. Li, and Z. Jiao, "An advanced distributed MDS-MAP localization algorithm with improved merging strategy," in *Proc. of IEEE ICIA 2016*.

[58] L. Zwirello, T. Schipper, M. Harter, and T. Zwick, "UWB localization system for indoor applications: Concept, realization and analysis," *Journal of Electrical and Computer Engineering*, vol. 2012, pp. 1–11, 2012.

[59] I. Guvenc, C.-C. Chong, and F. Watanabe, "NLoS identification and mitigation for UWB localization systems," in *2007 IEEE Wireless Communications and Networking Conference*. IEEE, 2007, pp. 1571–1576.

[60] L. Kapoor and S. Thakur, "A survey on brain tumor detection using image processing techniques," in *2017 7th International Conference on Cloud Computing, Data Science & Engineering-Confluence*. IEEE, 2017, pp. 582–585.

[61] Y. P. Loh, X. Liang, and C. S. Chan, "Low-light image enhancement using gaussian process for features retrieval," *Signal Processing: Image Communication*, vol. 74, pp. 175–190, 2019.

[62] Y. Zhao and N. Patwari, "Noise reduction for variance-based device-free localization and tracking," in *2011 8th Annual IEEE Communications Society Conference on Sensor, Mesh and Ad Hoc Communications and Networks*. IEEE, 2011, pp. 179–187.

[63] G. E. Sotak Jr and K. L. Boyer, "The laplacian-of-gaussian kernel: a formal analysis and design procedure for fast, accurate convolution and full-frame output," *Computer Vision, Graphics, and Image Processing*, vol. 48, no. 2, pp. 147–189, 1989.

[64] L. Xiao, H. Ouyang, and C. Fan, "An improved otsu method for threshold segmentation based on set mapping and trapezoid region intercept histogram," *Optik*, vol. 196, p. 163106, 2019.

[65] espressif, "Espressif - ESP32-S2 MCU," Accessed: July'23. [Online]. Available: https://www.espressif.com/en/products/socs/esp32-s2

[66] Qorvo, "MDEK1001 UWB Development Kit," Accessed: Jul'23. [Online]. Available: https://www.qorvo.com/products/p/MDEK1001

[67] M. I. Ribeiro, "Kalman and extended kalman filters: Concept, derivation and properties," *Institute for Systems and Robotics*, vol. 43, no. 46, pp. 3736–3741, 2004.

[68] N. Robotics, "0x-Delta," Accessed: Nov'23. [Online]. Available: https://www.nex-robotics.com/0x-delta/0x-delta.html

[69] SICK, "LMS111-10100," Accessed: Nov'23. [Online]. Available: https://www.sick.com/br/en/catalog/products/lidar-and-radar-sensors/lidar-sensors/lms1xx/lms111-10100/p/p109842

[70] M. Quigley, K. Conley, B. Gerkey, J. Faust, T. Foote, J. Leibs, R. Wheeler, A. Y. Ng *et al.*, "Ros: an open-source robot operating system," in *ICRA workshop on open source software*, vol. 3, no. 3.2. Kobe, Japan, 2009, p. 5.

[71] P.-S. Liao, T.-S. Chen, P.-C. Chung *et al.*, "A fast algorithm for multilevel thresholding," *Journal of Information Science and Engineering*, vol. 17, no. 5, pp. 713–727, 2001.

[72] G. Wang, W. Li, M. A. Zuluaga, R. Pratt, P. A. Patel, M. Aertsen, T. Doel, A. L. David, J. Deprest, S. Ourselin *et al.*, "Interactive medical image segmentation using deep learning with image-specific fine tuning," *IEEE Transactions on Medical Imaging*, vol. 37, no. 7, pp. 1562–1573, 2018.

[73] R. Chandel and G. Gupta, "Image filtering algorithms and techniques: A review," *International Journal of Advanced Research in Computer Science and Software Engineering*, vol. 3, no. 10, 2013.

[74] J. Luomala and I. Hakala, "Effects of temperature and humidity on radio signal strength in outdoor wireless sensor networks," in *Proc. of FedCSIS 2015*.

[75] Z. Yang, Z. Zhou, and Y. Liu, "From RSSI to CSI: Indoor localization via channel response," *ACM Computing Surveys (CSUR)*, vol. 46, no. 2, pp. 1–32, 2013.

[76] X. Zhao, Z. An, Q. Pan, and L. Yang, "NeRF2: Neural radio-frequency radiance fields," in *Proc. of ACM MOBICOM 2023.*

Amartya Basu received the B.Tech degree in computer science and engineering from Government College of Engineering and Leather Technology, Kolkata, India in 2020. He is currently pursuing the MS by Research degree in computer science and engineering at the Indian Institute of Technology (IIT) Madras, India. His research interest lies in the broad spectrum of wireless sensing focusing on radio frequency (RF) based imaging.

Ayon Chakraborty received the B.E. degree in computer science and engineering from Jadavpur University, India in 2011, and a Ph.D. degree in computer science from SUNY Stony Brook, NY, USA in 2017. Since 2020, he is with the Department of Computer Science and Engineering at Indian Institute of Technology (IIT) Madras, India where he currently serves as an Assistant Professor. Ayon is broadly interested in system-level design of future intelligent wireless systems and sensing technologies, spanning both algorithm design as well as system prototyping. He routinely serves on the Program Committees of top networking and mobile computing conferences.

Kush Jajal received the M.Tech degree in computer science from the Indian Institute of Technology, Madras, India in 2023. In 2023, he joined Nutanix as a Member of Technical Staff. His research interest lies in wireless sensing and deep learning.